Stability and Metastability of Li$_3$YCl$_6$ and Li$_3$HoCl$_6$

Hiroaki Ito,[a] Nakahira Yuki,[b] Naoki Ishimatsu,[c] Yosuke Goto,[d] Aichi Yamashita,[e] Yoshikazu

Mizuguchi,[e] Chikako Moriyoshi,[c] Takashi Toyao,[f] Ken-ichi Shimizu,[f] Hiroshi Oike,[g]

Masanori Enoki,[h] Nataly Carolina Rosero-Navarro,[i,j] Akira Miura,[j]* Kiyoharu Tadanaga[j]

[a] Graduate School of Chemical Science and Engineering, Hokkaido University, Kita 13, Nishi 8, Sapporo 060-8628, Japan.

[b] Quantum Beam Science Research Directorate, National Institutes for Quantum Science and Technology, Hyogo 679-5148, Japan

[c] Graduate School of Advanced Science and Engineering, Hiroshima University, 1-3-1 Kagamiyama, Higashihiroshima, 739-8526, Japan

[d] National Institute of Advanced Industrial Science and Technology (AIST), Tsukuba, Ibaraki 305-8568, Japan

[e] Department of Physics, Tokyo Metropolitan University, Hachioji 192-0397, Japan.

[f] Institute for Catalysis, Hokkaido University, Kita 21, Nishi 10, Sapporo, Hokkaido 001-0021, Japan

[g] PRESTO, Japan Science and Technology Agency, 4-1-8 Honcho, Kawaguchi 332-0012, Japan

[h] Institute of Multidisciplinary Research for Advanced Materials, Tohoku University, 2-1-1 Katahira, Aoba-ku, Sendai 980-8577, Japan

[i] Instituto de Cerámica y Vidrio (CSIC), Campus de Cantoblanco, 28049, Madrid, Spain.

[j] Faculty of Engineering, Hokkaido University, Kita 13, Nishi 8, Sapporo 060-8628, Japan.

Abstract

Metastable solid electrolytes exhibit superior conductivity compared to stable ones, making them a subject of considerable interest. However, solid-state synthesis of the metastable phase is affected by multiple thermodynamic and kinetic parameters, leading to ambiguity in the categorization of stability and metastability. This study categorizes remnant and intermediate metastability based on thermodynamic principles. The intermediate metastable phase, which is less stable than the temperature-independent stable phase, typically transforms into the stable phase(s) at high temperatures. In contrast, the remnant metastable phase, such as the high-temperature stable phase obtained by fast cooling, becomes the most stable phase, and annealing of the remnant metastable phase causes the phase transition to the low-temperature stable phase. Investigating Li^+ conducting chlorides, Li_3MCl_6 (M = Y and Ho), this study shows that heating starting materials to approximately 600 K produced low-temperature Li_3MCl_6 phase with one formula unit; high-temperature Li_3MCl_6 with three formula units were observed by further heating. Annealing of quenched Li_3MCl_6 at 573 K resulted in a phase transition from high-temperature to low-temperature, indicating that the high-temperature phase was remnant metastable at low temperatures. XRD patterns of low-temperature phases suggest the presence of stacking faults that stabilize low-temperature structures with high symmetry.

Introduction

Metastability provides a broad range of crystal and electronic structures and properties, leading to the fabrication of numerous functional solid-state materials, including superconductors,[1,2] catalysts,[3–5] superionic materials,[6–8] and electronic materials.[9,10] However, the synthesis of such metastable compounds often necessitates rigorous trial and error because the synthesis should be controlled not only thermodynamically but also kinetically. Studies on the prediction of the energy of inorganic solid-state synthesis using density functional theory (DFT) are in progress.[11–13] In situ analysis of the synthesis reactions provides another way to comprehend the existence and roles of intermediates before the formation of thermodynamically stable compounds.[13–22] Despite this, realizing a mechanism-based approach to the synthesis of predesigned inorganic metastable solids remains challenging.[23,24]

Because both kinetics and thermodynamics affect the metastability of solid-state reactions, determining the metastability of polymorphs requires comparing the free energy under different conditions. Martinolich and Neilson previously proposed the use of reaction coordinate diagrams, also known as "kinetic control and kinetic trapping"[25] as a necessary approach to stabilize metastable phases.

The metastable phase can be easily understood within a thermodynamic framework at a specific thermodynamic condition. However, when the thermodynamic condition changes, metastable phases can be categorized as intermediate or remnant metastable ones. Energy

diagrams of the intermediate and remnant metastable phases are presented in fig.1. In fig. 1a, the intermediate metastable phase has higher energies than the temperature-independent most stable phase at any temperature. This metastability is not the most stable phase during synthesis, and therefore the starting materials play a critical role in designing the reaction.[26] For example, an amorphous precursor with less-stable starting materials leads to the thermodynamically metastable polymorphs of Pb-Nb-Se[27] and Na_3N[28] In contrast, remnant metastable phases, a term introduced by Sun *et al*[29] are remnants of phases that were once the most stable at high temperatures and are obtained by quenching, which kinetically circumvents the phase transition to the low-temperature stable phase. Thus, this metastable phase becomes the most stable phase once, in contrast to intermediate metastability. Examples of remnant metastable materials include traditional silica-based glasses,[30,31] metallic glasses,[32] the recently developed high-entropy alloys,[5,33] and exotic electron states such as spin glasses.[10] Fig.1b illustrates the energy diagram of the low-temperature phase, high-temperature phase, and remnant metastable phase. Low-temperature and high-temperature phases are defined as stabilized phases at each thermodynamic condition. If the transition of the high-temperature phase to the low-temperature phase is circumvented through rapid cooling, the resulting polymorph observed at high temperatures may be considered a remnant metastable phase. Thus, the type of metastability of polymorphs in a given system cannot be determined solely by the first heating.
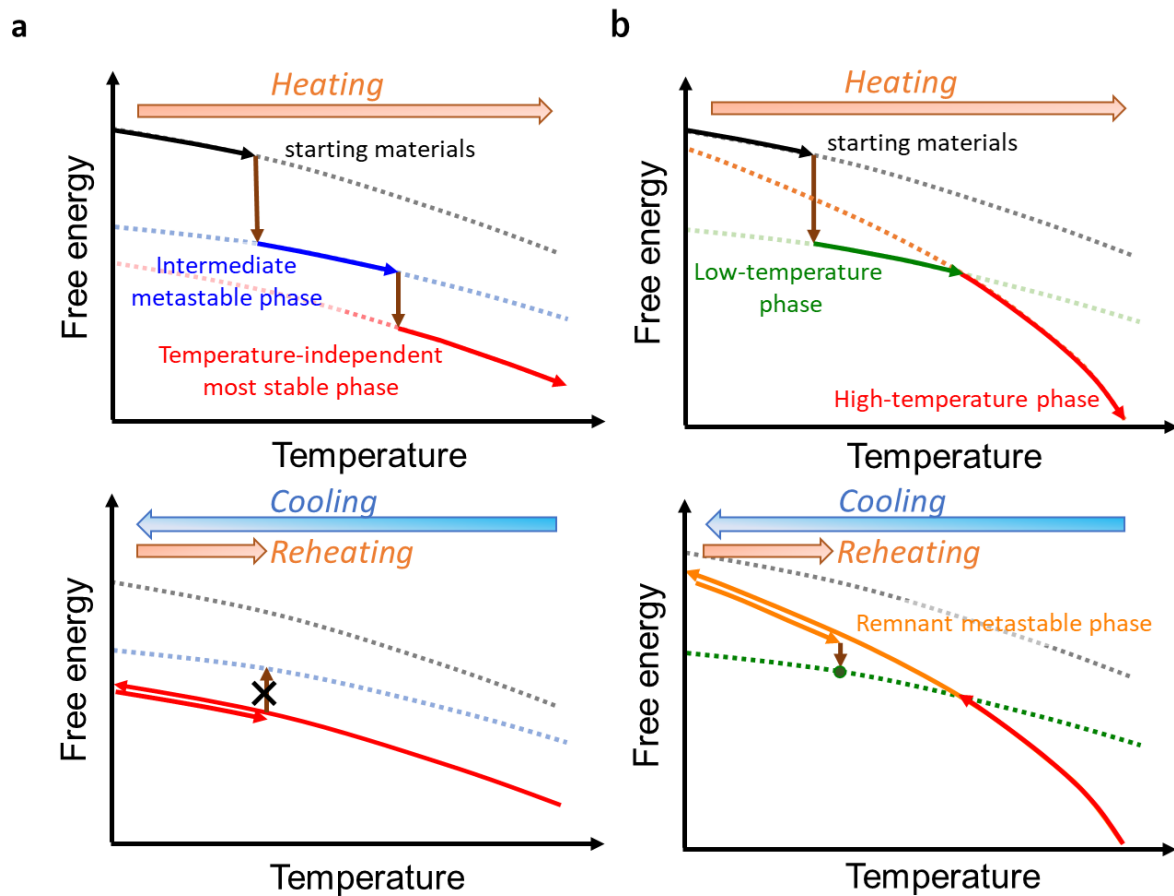
Fig. 1: Energy diagrams depicting intermediate metastability and remnant metastability.

(a) Intermediate metastable system in which the intermediate metastable product is located at an intermediate position. (b) Remnant metastable system in which the remnant metastable product is stabilized by high temperature.

The thermodynamic stability can be examined via thermal analysis. However, when the energy of these phases is close, the heat signal may not be detectable. In such cases, annealing at a lower temperature for an extended period is necessary to distinguish them. The decision tree to determine the type of (meta)stability is shown in Fig. 2. The intermediate metastable

phase cannot be formed from the stable phase, whereas the low-temperature phase can be

obtained by annealing the remnant metastable phase. Therefore, we can distinguish between the

pair of temperature-dependent stable and intermediate metastable phases or the remnant

metastable and low-temperature phases. Notably, the metastable phase is observed at a low

temperature in the former pair, while the metastable one in the latter pair appears at a high

temperature.
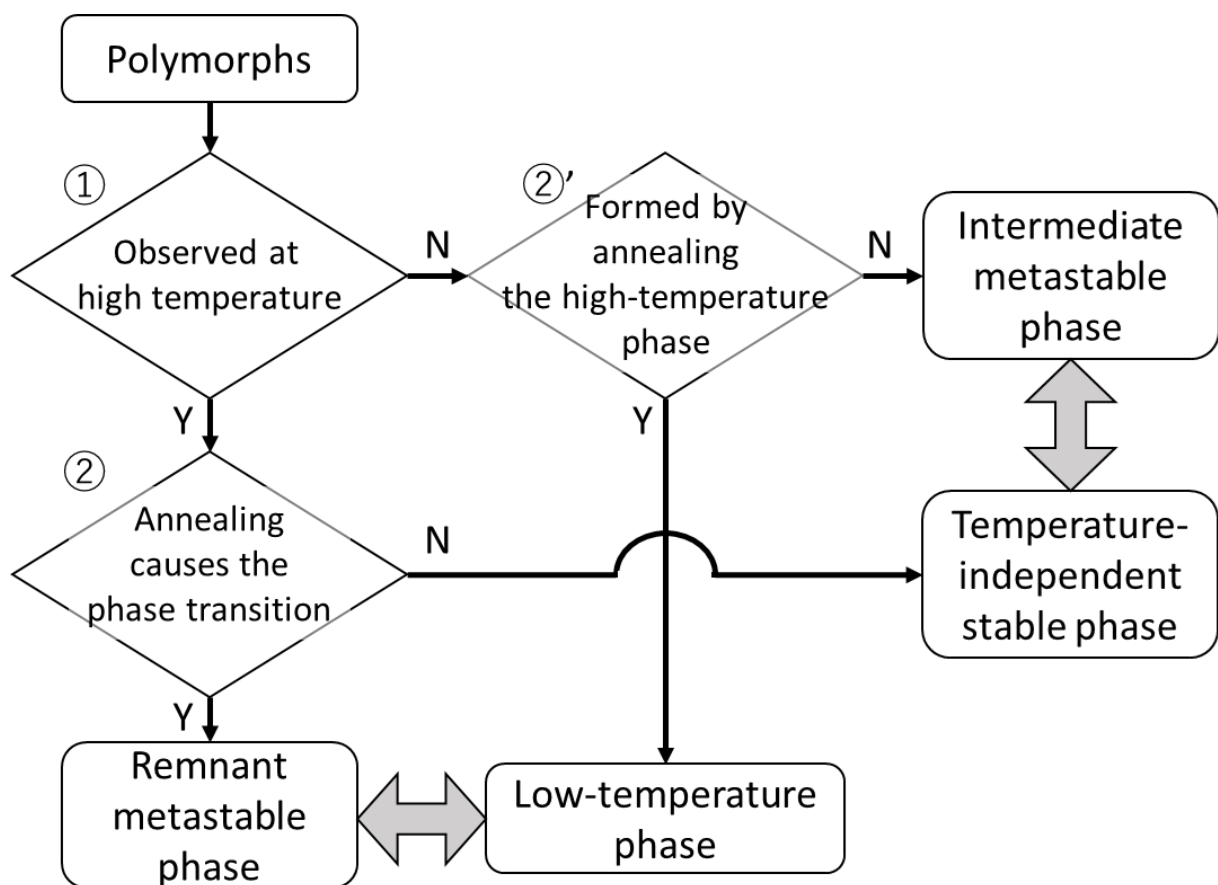
Fig. 2: Decision tree to determine the type of metastability. The system with intermediate

metastable and stable phases does not exhibit a transition before or after the annealing of the

quenched sample. However, a low-temperature phase can be formed by heating the remnant metastable phase obtained through rapid cooling.

Superionic conductors, which have been intensively studied for their potential application in all-solid-state batteries, constitute a class of materials that are particularly relevant for the study of metastable phases. Among these materials, the lithium ion-conducting Li_3MCl_6[34] (*M*: Sc,[35] Y,[36–39] In,[38,40] Dy,[41] Ho,[41,42] and Er[41,43]) is a noteworthy motif for investigating new structures and the nature of metastability (Table S1). Li_3MCl_6 can adopt diverse cation arrangements in the relatively simple hexagonal close-packed structure of Cl, indicating the possibility of various metastable states. The synthetic route employed for their preparation affects their structure.[36,37,39] Ball milling and subsequent heating produced low-crystallinity and crystallized samples of Li_3YCl_6.[36] Furthermore, cooling after heat treatment resulted in structural diversity, which was attributed to the formation of stacking faults and local structural changes.[37,39] In a previous report, we demonstrated that kinetically stabilized Li_3YCl_6 with different arrangements of Y could be obtained by low-temperature heating at 595 K.[14]

In this study, the type of metastability was categorized by the relative stabilities of polymorphs of Li_3YCl_6 and determined to discuss the structure-metastability-property relationship. The type of metastability of Li_3HoCl_6 with similar ionic radii and electronegativity of Y^{3+} were also investigated.

Experimental Methods

Li$_3$YCl$_6$ and Li$_3$HoCl$_6$ were synthesized by heating a mixture of LiCl, YCl$_3$, and HoCl$_3$ in a molar ratio of 3:1. The anhydrous reagents, LiCl, YCl$_3$, and Ho were procured from Kojyundo Chemical, Wako, and Aldrich, respectively. *In situ* synchrotron XRD patterns were collected at the BL02B2 beamline of SPring-8 with a temperature sweep rate of 30 K/min (Proposal number: 2019B1195, 2021B1175, 2022B0559, 2022A1698). Near-phase pure samples of the two polymorphs of Li$_3$YCl$_6$ were synthesized based on a previous study[15]. The samples were first heated at 700 K for 3–4 h and then cooled to 300 K by rapidly removing them from the furnace. Subsequently, they were subjected to further heating at 573–595 K for 50 h. XRD patterns were recorded at 300 K using CuKα radiation (Miniflex 600, RIGAKU) at the BL02B2 beamline of SPring-8. The crystal structures were refined using the RIETAN-FP[44] program and visualized using the VESTA[45] program.

XANES measurements of the Y, K, and Ho L_3 edges were performed at the Aichi Synchrotron Radiation Center BL5S1 (Proposal number: 2022D3006) and Spring-8BL14B2 (Proposal number: 2022A1736). The local structures surrounding Y and Ho were refined using Artemis. Solid-state NMR spectra of ^{7}Li were recorded on a 500 MHz Bruker NMR spectrometer with a magic angle spinning at 15 kHz. AC impedance measurements were performed using an Sl1260 impedance analyzer. The sample powders were uniaxially pressed at approximately 150 MPa, and cold-pressed pellets were placed between stainless steel plugs. The potential amplitude was set to 30 mV, and the frequency was swept from 10 to 100 Hz. The

conductivity was determined as the total resistivity, which includes both bulk and interface resistances.

Results and Discussion

Figure 3 displays the *in situ* XRD patterns of the mixture of LiCl and MCl_3 at different temperatures. Both sets of the LiCl-YCl_3 and LiCl-$HoCl_3$ mixtures formed different superstructures through a similar two-step reaction. LiCl and MCl_3 were designated as the starting materials. Peaks that can be indexed to Li_3MCl_6 (M = Y, Ho) with a simple structure were observed from 600 K onwards (Figure 3c). Upon heating, the $2\bar{1}0$ peak was observed, suggesting the formation of Li_3MCl_6 with a superlattice structure (Figure 3c, top). Henceforth, we shall refer to a simple Li_3MCl_6 structure with $Z = 1$ (where Z represents the number of formula units in the cell) as S-Li_3MCl_6 and a superlattice Li_3MCl_6 structure with $Z = 3$ as T-Li_3MCl_6. The 101 peaks were only observed for the T-phase because the corner of the unit cell was periodically occupied by the M cations. The stoichiometry of the S- and T- phases remained constant because of the constant M:Cl ratio (Table S2–3). Rietveld profiles for S- and T-Li_3HoCl_6 are shown in Figures S1 and S2.
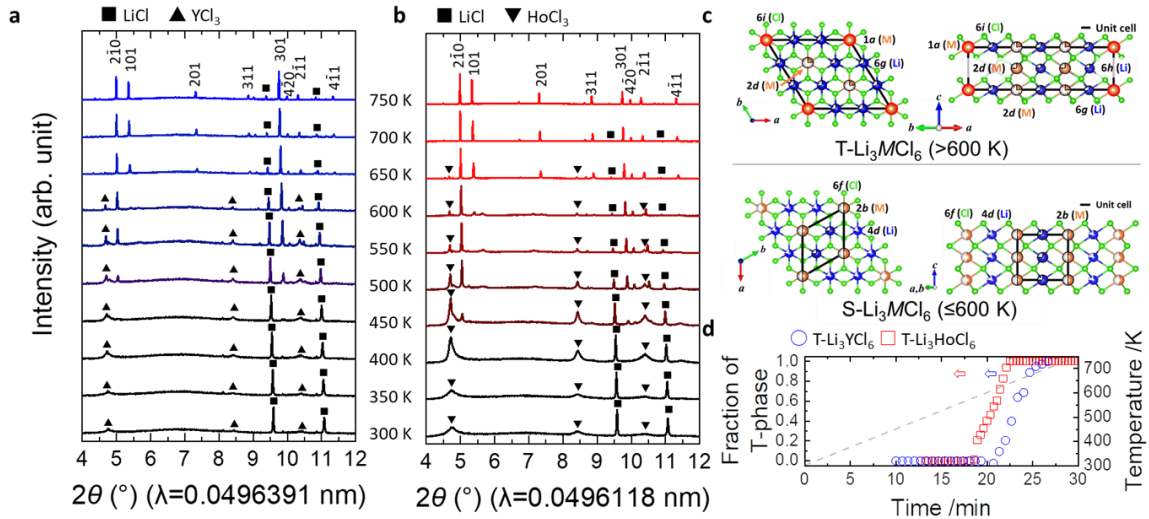
Fig. 3: Two-step synthesis of S-Li₃_M_Cl₆ and T-Li₃_M_Cl₆ monitored by in situ synchrotron XRD. (a, b) In situ XRD patterns for the reaction of LiCl and MCl₃ to produce Li₃MCl₆. Miller indices of T-Li₃MCl₆ are shown at the top. Products transformed from S-Li₃MCl₆ to T-Li₃MCl₆. (c) Crystal structures of S- and T-phases; unit cells are denoted using black lines. (d) Temperature profile and fractions of T-phase acquired from the Rietveld refinement of in situ XRD patterns. Diffraction data of Li₃YCl₆ are reproduced using a previous study [14].

To classify the type of metastability, the reversibility of the phase transition of Li₃MCl₆ was investigated. Figures **4a** and **4b** display the XRD patterns of T-Li₃YCl₆ and T-Li₃HoCl₆ before and after low-temperature annealing at 573 K. Before annealing, all the peaks were indexed to T-phases and the residual LiCl. The relative intensities of the 101 peaks against 2$\bar{1}$0 peaks of Li₃YCl₆ and Li₃HoCl₆ decreased after annealing at 573 K, indicating that T-Li₃MCl₆ transformed to S-Li₃MCl₆. The two peaks at 2θ values at 5.5 and 7.5 ° can be attributed to the stacking faults along the c-axis, as previously reported by E. Sebti et al.[39] The formation of stacking faults can stabilize the S-phase at low temperatures.

10
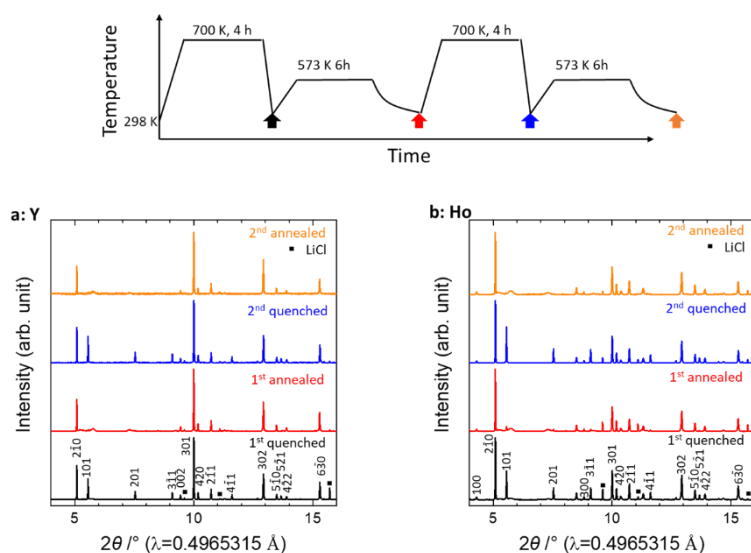
Fig. 4: Reversibility of phase transition from T-Li₃*M*Cl₆ to S-Li₃*M*Cl₆. XRD patterns of (a) T-Li₃YCl₆ and (b) T-Li₃HoCl₆ before and after annealing at 595 and 573 K for 50 h. A decrease in the intensity of the 101 peaks of T-Li₃HoCl₆ upon annealing indicated the formation of the S-phase.

The reversible phase transition from S-Li₃*M*Cl₆ to T-Li₃*M*Cl₆ suggests that S-Li₃*M*Cl₆ is a low-temperature stable phase at lower temperatures below 600 K, while T-Li₃*M*Cl₆ is a remnant metastable phase at temperatures ranging from 300 to 600 K, and becomes stable at higher temperatures. Notably, the type of metastability observed in ionic Li₃*M*Cl₆ with similar ionic radii and electronegativity[46] of Y^{3+} and Ho^{3+} was observed to be the same.

To gain further insights into the underlying causes of the observed metastability, the EXAFS of Y and Ho and the NMR spectra of Li^7 were recorded. The XAFS measurements revealed that the local structures of Y and Ho were not affected by the Li₃YCl₆ or Li₃HoCl₆ polymorph.

However, the NMR data suggested a slight difference in the local structure of Li^+ between the two polymorphs.

The Y K-edge and Ho L_3-edge of both S- and T-Li_3HoCl_6 were also analyzed (Figure S3–4). The obtained EXAFS spectra of S- and T-Li_3YCl_6 were found to be comparable (Figure **5a**), as were the profiles of S- and T-Li_3HoCl_6. The Fourier-transformed EXAFS data of S-Li_3YCl_6 were well-fitted with the simulated data based on the model without the nearest-neighboring Y-Y, as illustrated in the inset of Figure **5b**. The refinement of Li_3HoCl_6 also suggested that the nearest neighboring Ho-Ho did not exist in the structure (see Supporting Information). Accordingly, a structural model comprising 1D atomic chains with alternate Y and Ho species was proposed (Figure **5c**). The structural models derived based on EXAFS and XRD measurements are shown in Figure **5d**. The difference between S- and T-Li_3YCl_6 reflects in the periodicity of the different lattices. In the T-phase, Y is located at the lattice corner, whereas in the S-phase, Y loses this periodicity. This periodicity was observed as the 101 diffraction peak in the XRD pattern, as described earlier.
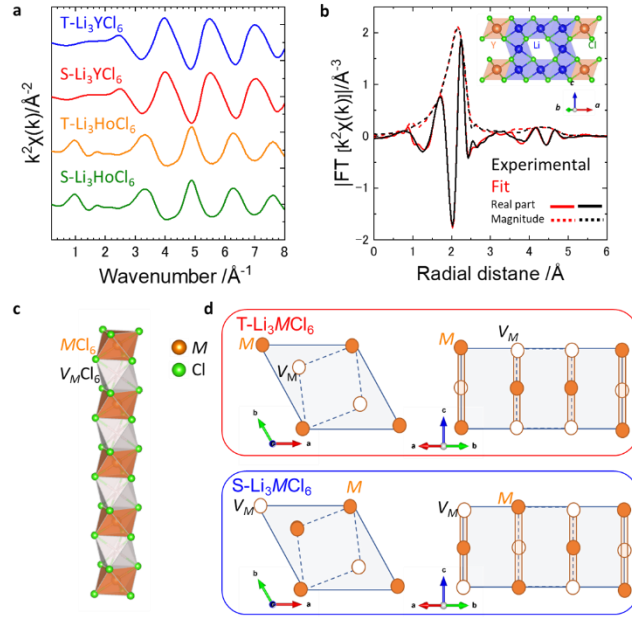
Fig. 5: Local structure of Y or Ho in Li$_3M$Cl$_6$. (a) EXAFS spectra of Li$_3M$Cl$_6$. (b) Fourier transform of EXAFS analysis of T-Li$_3$YCl$_6$; inset shows the structure model for XANES derived from XRD. (c) Schematic image of the MCl$_6$-V_MCl$_6$-MCl$_6$ chain along the c-axis. V_M denotes the vacancy at the M site. (d) Schematic image of the arrangement of chains in S- and T-Li$_3M$Cl$_6$.

The ^{7}Li NMR spectra of different Li$_3M$Cl$_6$ polymorphs suggest distinct differences between them, which contrasts with the findings of the X-ray absorption spectra. The peak positions were found to be different (Figure 6 and Figure S5 (for a longer range)), with S-Li$_3$YCl$_6$, T-Li$_3$YCl$_6$, T-Li$_3$HoCl$_6$, and S-Li$_3$HoCl$_6$ exhibiting a peak at -0.80 ppm, -0.89 ppm, -1.26 ppm, and -1.48 ppm, respectively. The negative shift in the peak indicates a lower electronic density around Li. The sharpest peak was observed for T-Li$_3$YCl$_6$, followed by S-Li$_3$YCl$_6$, whereas the

peaks for T- and S-Li$_3$HoCl$_6$ were broad. The widths of these peaks suggest that the number of sites where Li can exist is greater in S-Li$_3$YCl$_6$ than in T-Li$_3$YCl$_6$. Additionally, the broader peaks for S- and T-Li$_3$HoCl$_6$ can be attributed to the magnetism induced because of the unpaired electrons in trivalent Ho^{3+}.[47]
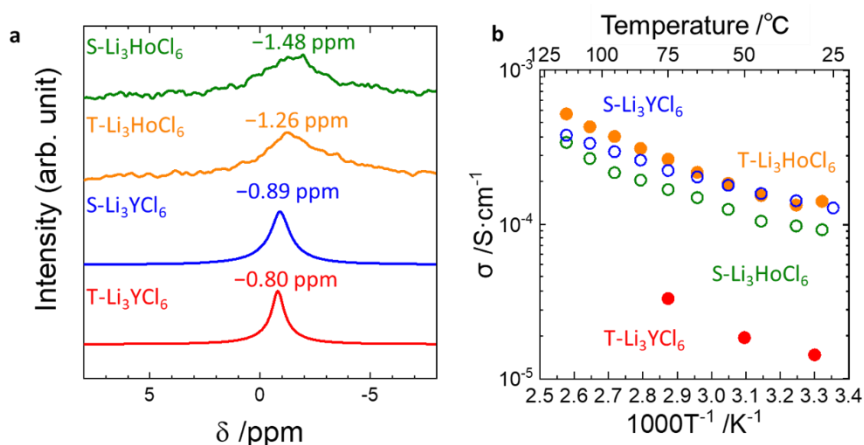
Fig. 6: Deviation of the local structure surrounding Li in Li$_3$MCl$_6$ and Li-ion conductivity of S- and T-Li$_3$MCl$_6$. (a) Solid-state ^{7}Li NMR spectra of S- and T-Li$_3$MCl$_6$. (b) Arrhenius plot of Li$^+$ conductivity of S- and T-Li$_3$MCl$_6$ determined using AC impedance measurements. The conductivities of S- and T-Li$_3$YCl$_6$ are reproduced from a previous study.[14]

To gain insights into the change in the Li environment, the conductivity of Li$^+$ was evaluated via AC impedance measurements. The ionic conductivities of the metastable T- and stable S-phase, represented by filled and non-filled circles, respectively, were determined. The ionic conductivities and activation energies of Li$^+$ conduction for T-Li$_3$HoCl$_6$ were 0.14 mS·cm^{-1} and 18 kJ/mol, respectively. These values were observed to be higher and smaller than those for S-Li$_3$HoCl$_6$, which were 0.092 mS·cm^{-1} and 14 kJ/mol, respectively.

14

The remnant metastable T-Li$_3M$Cl$_6$ and low-temperature stable S-Li$_3M$Cl$_6$ suggest a reversible behavior. A summary of the properties of these phases is presented in Table 1. Although the Y position exhibits ordered and disordered behavior in the T-phase and S-phase, respectively, the local ordering of vacancies of the Y site is similar. Furthermore, while the lattice volume per formula unit of S-Li$_3$YCl$_6$ was larger than that of T- Li$_3$YCl$_6$, the lattice volume of S-Li$_3$HoCl$_6$ was smaller than that of T-Li$_3$HoCl$_6$. In both cases, larger lattice parameters may account for higher ion conductivity through weak interaction between Li$^+$ and Cl$^-$. In the simple ionic model that is generally suitable for ionic chlorides with relatively simple structures, larger lattice parameters indicate metastable nature because of weak ionic bonding in Li$_3M$Cl$_6$. However, the energy estimated by the small lattice volume of metastable T-Li$_3$HoCl$_6$ cannot explain its metastable nature, in contrast to the case of T-Li$_3$YCl$_6$ with a large volume. Therefore, additional parameters that may affect stability need to be considered. One possible explanation would be the stabilization by stacking faults, which are suggested by broad diffraction peaks in both S- Li$_3$YCl$_6$ and S-Li$_3$HoCl$_6$ (Figure 3). Further investigation is required to quantitatively analyze the stacking faults and their effect on stability.

Table 1. Properties of Li$_3$YCl$_6$ and Li$_3$HoCl$_6$

	S-Li$_3$YCl$_6$	T-Li$_3$YCl$_6$	S-Li$_3$HoCl$_6$	T-Li$_3$HoCl$_6$
Stability at ambient temperature and pressure	Low-temperature stable	Remnant metastable	Low-temperature stable	Remnant metastable

Synthesis method	Heating at 595 K	Quenching at 700 K	Heating at 700 K and annealing at 500 K	Quenching at 700 K
Number of formula units per unit cell (Z)	1	3	1	3
Lattice Volume per formula unit /$\text{Å}^3 \cdot \text{Li}_3 M\text{Cl}_6$	217.962(7)	217.638(5)	218.278(9)	218.434(7)
Local Structure of M	$M\text{Cl}_6$-$V_M\text{Cl}_6$-$M\text{Cl}_6$	$M\text{Cl}_6$-$V_M\text{Cl}_6$-$M\text{Cl}_6$	$M\text{Cl}_6$-$V_M\text{Cl}_6$-$M\text{Cl}_6$	$M\text{Cl}_6$-$V_M\text{Cl}_6$-$M\text{Cl}_6$
Li^+ Conductivity ($\text{mS}\cdot\text{cm}^{-1}$)	0.12	0.014	0.092	0.14

Conclusion

In this study, remnant and intermediate metastability were introduced and the free energy curves of these metastabilities were depicted. Additionally, a decision tree was proposed to determine the metastability theoretically. Through the annealing process of $\text{Li}_3 M\text{Cl}_6$, the phase transition was established to be reversible. The high-temperature stable phase of $\text{Li}_3 M\text{Cl}_6$, referred to as T-$\text{Li}_3 M\text{Cl}_6$, was observed to be remnant metastable at low temperatures (below 573 K). Furthermore, annealing produced low-temperature stable S-$\text{Li}_3 M\text{Cl}_6$, which contained several defects in the crystal structure.

As a general conclusion, the importance of defining metastability was emphasized. While the terms "high-temperature" and "low-temperature" phases are commonly used, they lack a clear definition of thermodynamic stability. Using the words "high-temperature stable phase" and "low-temperature stable phase" to better define stability and subsequently define metastability

is preferable. Notably, temperature is one of the many thermodynamic parameters, and any other thermodynamic or multiple thermodynamic parameters, including pressure and magnetic field, can be used to understand intermediate and remnant metastability. In cases where the energy differences of thermodynamically competing phases are small, local structures and stacking faults can be critical factors in determining thermodynamic stability. Despite the discovery of stacking faults in several systems, the thermodynamic stability of complicated, layered structures is not yet fully understood.[27] To fully comprehend the thermodynamic stability of such structures, establishing clear definitions and utilizing accurate and quantitative structure analysis related to thermodynamic parameters is essential. This will also enable the rational design of metastable polymorphs.

AUTHOR INFORMATION

Corresponding Author: amiura@eng.hokudai.ac.jp

REFERENCES

1   Sleight, A. W., Synthesis of Oxide Superconductors, *Phys. Today* 1991, *44*, 24. DOI:

10.1063/1.881303.

2   Oike, H.; Kamitani, M.; Tokura, Y.; Kagawa, F., Kinetic Approach to

Superconductivity Hidden behind a Competing Order, *Sci. Adv.* 2018, *4*, eaau3489. DOI:

10.1126/sciadv.aau3489.

3   Tan, X.; Geng, S.; Ji, Y.; Shao, Q.; Zhu, T.; Wang, P.; Li, Y.; Huang, X., Closest

Packing Polymorphism Interfaced Metastable Transition Metal for Efficient Hydrogen

Evolution, *Adv. Mater.* 2020, *32*, e2002857. DOI: 10.1002/adma.202002857.

4   Cheetham, A. K., Advanced Inorganic Materials: An Open Horizon, *Science* 1994,

264, 794. DOI: 10.1126/science.264.5160.794.

5   Yao, Y.; Huang, Z.; Xie, P.; Lacey, S. D.; Jacob, R. J.; Xie, H.; Chen, F.; Nie, A.; Pu,

T.; Rehwoldt, M.; Yu, D.; Zachariah, M. R.; Wang, C.; Shahbazian-Yassar, R.; Li, J.; Hu, L.,

Carbothermal Shock Synthesis of High-Entropy-Alloy Nanoparticles, *Science* 2018, *359*, 1489.

DOI: 10.1126/science.aan5412.

6   Tatsumisago, M.; Shinkuma, Y.; Minami, T., Stabilization of Superionic α-Agl at

Room Temperature in a Glass Matrix, *Nature* 1991, *354*, 217. DOI: 10.1038/354217a0.

7   Kaup, K.; Zhou, L.; Huq, A.; Nazar, L. F., Impact of the Li Substructure on the Diffusion Pathways in Alpha and Beta Li_3PS_4: An *In Situ* High Temperature Neutron Diffraction Study, *J. Mater. Chem. A* 2020, *8*, 12446. DOI: 10.1039/D0TA02805C.

8   Kanazawa, K.; Yubuchi, S.; Hotehama, C.; Otoyama, M.; Shimono, S.; Ishibashi, H.; Kubota, Y.; Sakuda, A.; Hayashi, A.; Tatsumisago, M., Mechanochemical Synthesis and Characterization of Metastable Hexagonal Li_4SnS_4 Solid Electrolyte, *Inorg. Chem.* 2018, *57*, 9925. DOI: 10.1021/acs.inorgchem.8b01049.

9   Karube, K.; White, J. S.; Reynolds, N.; Gavilano, J. L.; Oike, H.; Kikkawa, A.; Kagawa, F.; Tokunaga, Y.; Rønnow, H. M.; Tokura, Y.; Taguchi, Y., Robust Metastable Skyrmions and Their Triangular-Square Lattice Structural Transition in a High-Temperature Chiral Magnet, *Nat. Mater.* 2016, *15*, 1237. DOI: 10.1038/nmat4752.

10   Kagawa, F.; Oike, H., Quenching of Charge and Spin Degrees of Freedom in Condensed Matter, *Adv. Mater.* 2017, *29*. DOI: 10.1002/adma.201601979.

11   McDermott, M. J.; Dwaraknath, S. S.; Persson, K. A., A Graph-Based Network for Predicting Chemical Reaction Pathways in Solid-State Materials Synthesis, *Nat. Commun.* 2021, *12*, 3097. DOI: 10.1038/s41467-021-23339-x.

12   Aykol, M.; Montoya, J. H.; Hummelshøj, J., Rational Solid-State Synthesis Routes for Inorganic Materials, *J. Am. Chem. Soc.* 2021, *143*, 9244. DOI: 10.1021/jacs.1c04888.

13   Miura, A.; Bartel, C. J.; Goto, Y.; Mizuguchi, Y.; Moriyoshi, C.; Kuroiwa, Y.; Wang, Y.; Yaguchi, T.; Shirai, M.; Nagao, M.; Rosero-Navarro, N. C.; Tadanaga, K.; Ceder, G.; Sun, W., Observing and Modeling the Sequential Pairwise Reactions That Drive Solid-State Ceramic Synthesis, *Adv. Mater.* 2021, *33*, e2100312. DOI: 10.1002/adma.202100312.

14   Ito, H.; Shitara, K.; Wang, Y.; Fujii, K.; Yashima, M.; Goto, Y.; Moriyoshi, C.; Rosero-Navarro, N. C.; Miura, A.; Tadanaga, K., Kinetically Stabilized Cation Arrangement in Li_3YCl_6 Superionic Conductor during Solid-State Reaction, *Adv. Sci. (Weinh)* 2021, *8*, e2101413. DOI: 10.1002/advs.202101413.

15   Haynes, A. S.; Stoumpos, C. C.; Chen, H.; Chica, D.; Kanatzidis, M. G., Panoramic Synthesis as an Effective Materials Discovery Tool: The System Cs/Sn/P/Se as a Test Case, *J. Am. Chem. Soc.* 2017, *139*, 10814. DOI: 10.1021/jacs.7b05423.

16   Bianchini, M.; Wang, J.; Clément, R. J.; Ouyang, B.; Xiao, P.; Kitchaev, D.; Shi, T.; Zhang, Y.; Wang, Y.; Kim, H.; Zhang, M.; Bai, J.; Wang, F.; Sun, W.; Ceder, G., The Interplay between Thermodynamics and Kinetics in the Solid-State Synthesis of Layered Oxides, *Nat. Mater.* 2020, *19*, 1088. DOI: 10.1038/s41563-020-0688-6.

17   He, H.; Yee, C.-H. H.; McNally, D. E.; Simonson, J. W.; Zellman, S.; Klemm, M.; Kamenov, P.; Geschwind, G.; Zebro, A.; Ghose, S.; Bai, J.; Dooryhee, E.; Kotliar, G.; Aronson, M. C., Combined Computational and Experimental Investigation of the $La_2CuO_{4-X}S_x$ ($0 \leq x \leq$

4) Quaternary System, *Proc. Natl Acad. Sci. U. S. A.* 2018, *115*, 7890. DOI: 10.1073/pnas.1800284115.

18   Kohlmann, H., Looking into the Black Box of Solid-State Synthesis, *Eur. J. Inorg. Chem.* 2019, 2019, 4174. DOI: 10.1002/ejic.201900733.

19   Nielsen, M. H.; Aloni, S.; De Yoreo, J. J., In Situ TEM Imaging of $CaCO_3$ Nucleation Reveals Coexistence of Direct and Indirect Pathways, *Science* 2014, *345*, 1158. DOI: 10.1126/science.1254051.

20   Jiang, Z.; Ramanathan, A.; Shoemaker, D. P., In Situ Identification of Kinetic Factors That Expedite Inorganic Crystal Formation and Discovery, *J. Mater. Chem. C* 2017, *5*, 5709. DOI: 10.1039/C6TC04931A.

21   Martinolich, A. J.; Kurzman, J. A.; Neilson, J. R., Circumventing Diffusion in Kinetically Controlled Solid-State Metathesis Reactions, *J. Am. Chem. Soc.* 2016, *138*, 11031. DOI: 10.1021/jacs.6b06367.

22   Kamm, G. E.; Huang, G.; Vornholt, S. M.; McAuliffe, R. D.; Veith, G. M.; Thornton, K. S.; Chapman, K. W., Relative Kinetics of Solid-State Reactions: The Role of Architecture in Controlling Reactivity, *J. Am. Chem. Soc.* 2022, *144*, 11975. DOI: 10.1021/jacs.2c05043.

23   DiSalvo, F. J., Solid-State Chemistry: A Rediscovered Chemical Frontier, *Science* 1990, *247*, 649. DOI: 10.1126/science.247.4943.649.

24   Chamorro, J. R.; McQueen, T. M., Progress Toward Solid State Synthesis by Design, *Acc. Chem. Res.* 2018, *51*, 2918. DOI: 10.1021/acs.accounts.8b00382.

25   Martinolich, A. J.; Neilson, J. R., Toward Reaction-by-Design: Achieving Kinetic Control of Solid State Chemistry with Metathesis, *Chem. Mater.* 2017, *29*, 479. DOI: 10.1021/acs.chemmater.6b04861.

26   Cordova, D. L. M.; Johnson, D. C., Synthesis of Metastable Inorganic Solids with Extended Structures, *ChemPhysChem* 2020, *21*, 1345. DOI: 10.1002/cphc.202000199.

27   Esters, M.; Alemayehu, M. B.; Jones, Z.; Nguyen, N. T.; Anderson, M. D.; Grosse, C.; Fischer, S. F.; Johnson, D. C., Synthesis of Inorganic Structural Isomers by Diffusion-Constrained Self-Assembly of Designed Precursors: A Novel Type of Isomerism, *Angew. Chem. Int Ed Engl* 2015, *54*, 1130. DOI: 10.1002/anie.201409714.

28   Mizoguchi, H.; Park, S. W.; Katase, T.; Vazhenin, G. V.; Kim, J.; Hosono, H., Origin of Metallic Nature of Na_3N, *J. Am. Chem. Soc.* 2021, *143*, 69. DOI: 10.1021/jacs.0c11047.

29   Sun, W.; Dacek, S. T.; Ong, S. P.; Hautier, G.; Jain, A.; Richards, W. D.; Gamst, A. C.; Persson, K. A.; Ceder, G., The Thermodynamic Scale of Inorganic Crystalline Metastability, *Sci. Adv.* 2016, *2*, e1600225. DOI: 10.1126/sciadv.1600225.

30   Shelby, J. E., Introduction to Glass Science and Technology, The Royal Society of Chemistry, 2005. DOI: 10.1039/9781847551160.

31   Klement, W.; Willens, R. H.; Duwez, P. O. L., Non-crystalline Structure in Solidified Gold-Silicon Alloys, *Nature* 1960, *187*, 869. DOI: 10.1038/187869b0.

32   Sheng, H. W.; Luo, W. K.; Alamgir, F. M.; Bai, J. M.; Ma, E., Atomic Packing and Short-to-Medium-Range Order in Metallic Glasses, *Nature* 2006, *439*, 419. DOI: 10.1038/nature04421.

33   Evans, D.; Chen, J.; Bokas, G.; Chen, W.; Hautier, G.; Sun, W., Visualizing Temperature-Dependent Phase Stability in High Entropy Alloys, *npj Comput. Mater.* 2021, *7*, 1. DOI: 10.1038/s41524-021-00626-1.

34   Kwak, H.; Wang, S.; Park, J.; Liu, Y.; Kim, K. T.; Choi, Y.; Mo, Y.; Jung, Y. S., Emerging Halide Superionic Conductors for All-Solid-State Batteries: Design, Synthesis, and Practical Applications, *ACS Energy Lett.* 2022, 7, 1776. DOI: 10.1021/acsenergylett.2c00438.

35   Liang, J.; Li, X.; Wang, S.; Adair, K. R.; Li, W.; Zhao, Y.; Wang, C.; Hu, Y.; Zhang, L.; Zhao, S.; Lu, S.; Huang, H.; Li, R.; Mo, Y.; Sun, X., Site-Occupation-Tuned Superionic Li_xScCl_{3+x} Halide Solid Electrolytes for All-Solid-State Batteries, *J. Am. Chem. Soc.* 2020, 142, 7012. DOI: 10.1021/jacs.0c00134.

36   Asano, T.; Sakai, A.; Ouchi, S.; Sakaida, M.; Miyazaki, A.; Hasegawa, S., Solid Halide Electrolytes with High Lithium-Ion Conductivity for Application in 4 V Class Bulk-Type All-Solid-State Batteries, *Adv. Mater.* 2018, *30*, e1803075. DOI: 10.1002/adma.201803075.

37   Schlem, R.; Banik, A.; Ohno, S.; Suard, E.; Zeier, W. G., Insights into the Lithium Sub-structure of Superionic Conductors Li_3YCl_6 and Li_3YBr_6, *Chem. Mater.* 2021, *33*, 327. DOI: 10.1021/acs.chemmater.0c04352.

38   Steiner, H.-J.; Lutz, H. D., Neue Schnelle Ionenleiter vom Typ $M_3^IM^{III}Cl_6$ (M^I = Li, Na, Ag; M^{III} = In, Y), *Z. Anorg. Allg. Chem.* 1992, *613*, 26. DOI: 10.1002/zaac.19926130104.

39   Sebti, E.; Evans, H. A.; Chen, H.; Richardson, P. M.; White, K. M.; Giovine, R.; Koirala, K. P.; Xu, Y.; Gonzalez-Correa, E.; Wang, C.; Brown, C. M.; Cheetham, A. K.; Canepa, P.; Clément, R. J., Stacking Faults Assist Lithium-Ion Conduction in a Halide-Based Superionic Conductor, *J. Am. Chem. Soc.* 2022, *144*, 5795. DOI: 10.1021/jacs.1c11335.

40   Li, X.; Liang, J.; Chen, N.; Luo, J.; Adair, K. R.; Wang, C.; Banis, M. N.; Sham, T. K.; Zhang, L.; Zhao, S.; Lu, S.; Huang, H.; Li, R.; Sun, X., Water-Mediated Synthesis of a Superionic Halide Solid Electrolyte, *Angew. Chem. Int Ed Engl* 2019, *58*, 16427. DOI: 10.1002/anie.201909805.

41   Bohnsack, A.; Stenzel, F.; Zajonc, A.; Balzer, G.; Wickleder, M. S.; Meyer, G., Ternäre Halogenide vom Typ A_3MX_6. VI [1]. Ternäre Chloride Der Selten-Erd-Elemente mit Lithium, Li_3MCl_6 (M = Tb–Lu, Y, Sc): Synthese, Kristallstrukturen und Ionenbewegung, *Z. Anorg. Allg. Chem.* 1997, *623*, 1067. DOI:10.1002/zaac.19976230710.

42   Liang, J.; Maas, E.; Luo, J.; Li, X.; Chen, N.; Adair, K. R.; Li, W.; Li, J.; Hu, Y.; Liu, J.; Zhang, L.; Zhao, S.; Lu, S.; Wang, J.; Huang, H.; Zhao, W.; Parnell, S.; Smith, R. I.; Ganapathy, S.; Wagemaker, M.; Sun, X., A Series of Ternary Metal Chloride Superionic Conductors for High-Performance All-Solid-State Lithium Batteries, *Adv. Energy Mater.* 2022, *12*, 2103921. DOI: 10.1002/aenm.202103921.

43   Muy, S.; Voss, J.; Schlem, R.; Koerver, R.; Sedlmaier, S. J.; Maglia, F.; Lamp, P.; Zeier, W. G.; Shao-Horn, Y., High-Throughput Screening of Solid-State Li-Ion Conductors Using Lattice-Dynamics Descriptors. *iScience* 2019, *iScience* 2019, *16*, 270. DOI: 10.1016/j.isci.2019.05.036.

44   Izumi, F.; Momma, K., Three-Dimensional Visualization in Powder Diffraction, *Solid State Phenom.* 2007, *130*, 15. DOI: 10.4028/www.scientific.net/SSP.130.15.

45   Momma, K.; Izumi, F., *VESTA 3* for Three-Dimensional Visualization of Crystal, Volumetric and Morphology Data, *J. Appl. Crystallogr.* 2011, *44*, 1272. DOI: 10.1107/S0021889811038970.

46   Shannon, R. D., Revised Effective Ionic Radii and Systematic Studies of Interatomic Distances in Halides and Chalcogenides, *Acta Cryst. A* 1976, *32*, 751. DOI: 10.1107/S0567739476001551.

47   Peng, L.; Clément, R. J.; Lin, M.; Yang, Y., CHAPTER 1, NMR Principles of Paramagnetic Materials, 2021, pp. 1–70. DOI: 10.1039/9781839160097-00001.

Supporting Documents: Stability and Metastability of Li_3YCl_6 and Li_3HoCl_6

Hiroaki Ito,[a] Nakahira Yuki,[b] Naoki Ishimatsu,[c] Yosuke Goto,[d] Aichi Yamashita[e] Yoshikazu

Mizuguchi,[e] Chikako Moriyoshi,[c] Takashi Toyao,[f] Ken-ichi Shimizu,[f] Hiroshi Oike,[g]

Masanori Enoki,[h] Nataly Carolina Rosero-Navarro,[i,j] Akira Miura,[j]* Kiyoharu Tadanaga[j]

Corresponding author: Akira Miura amiura@eng.hokudai.ac.jp

[a] Graduate School of Chemical Science and Engineering, Hokkaido University, Kita 13, Nishi 8, Sapporo 060-8628, Japan.

[b] Quantum Beam Science Research Directorate, National Institutes for Quantum Science and Technology, Hyogo 679-5148, Japan

[c] Graduate School of Advanced Science and Engineering, Hiroshima University, 1-3-1 Kagamiyama, Higashihiroshima, 739-8526, Japan

[d] National Institute of Advanced Industrial Science and Technology (AIST), Tsukuba, Ibaraki 305-8568, Japan

[e] Department of Physics, Tokyo Metropolitan University, Hachioji 192-0397, Japan.

[f] Institute for Catalysis, Hokkaido University, Kita 21, Nishi 10, Sapporo, Hokkaido 001-0021, Japan

[g] PRESTO, Japan Science and Technology Agency, 4-1-8 Honcho, Kawaguchi 332-0012, Japan

[h] Institute of Multidisciplinary Research for Advanced Materials, Tohoku University, 2-1-1 Katahira, Aoba-ku, Sendai 980-8577, Japan

[i] Instituto de Cerámica y Vidrio (CSIC), Campus de Cantoblanco, 28049, Madrid, Spain.

[j] Faculty of Engineering, Hokkaido University, Kita 13, Nishi 8, Sapporo 060-8628, Japan.

Table S1 shows examples of synthesis methods and structural features of chlorides, Li_3MCl_6, with trivalent M^{3+} cations.

Table S1 Reports of synthesis methods and features of chloride Li_3MCl_6

| Ref.	Composition	Synthesis method	Feature
37	Li_3YCl_6	Ball-milling and heating	Low crystallinity
38	Li_3YCl_6	Ball-milling and heating	Different Y arrangements in the cell
39	Li_3YCl_6	Heating	First report
	Li_3InCl_6	Heating	First report
40	Li_3YCl_6	Ball-milling and heating	Stacking fault
41	Li_3InCl_6	Drying of solution	First report of the solution process
	Li_3DyCl_6	Heating	First report
42	Li_3HoCl_6	Heating	First report
	Li_3ErCl_6	Heating	First report
43	$Li_{3-3x}Ho_{1+x}Cl_6$	Heating	Defect introduction
44	Li_3ErCl_6	Heating	Calculation

Fig. S1 and S2 show the Rietveld profiles of S- and T-Li_3HoCl_6. The samples were synthesized by heating at 700 K and quenching or slow cooling, and the XRD patterns were measured at 300 K.

Fig. S1 shows the profile for S-Li_3HoCl_6. The main peaks were indexed as the S-phase while weak peaks of law materials were observed. The red-cross marks indicate the experimental results, and the green line corresponds to the simulated pattern. The refinement parameters converged with moderate values. The lattice parameters, atomic positions, and thermal displacement parameters are listed in Table S2. Figure S2 shows the profile for T-Li_3HoCl_6. With minor peaks of LiCl and $HoCl_6$, all peaks were indexed as T-phase. The refined crystallographic parameters are listed in Table S3. As discussed in the paper, the T-Li_3HoCl_6 exhibited a larger volume per the formula unit than that of S-Li_3HoCl_6.

$R_{wp}=20.006\%$
$R_p=12.208\%$
$S=14.6700$
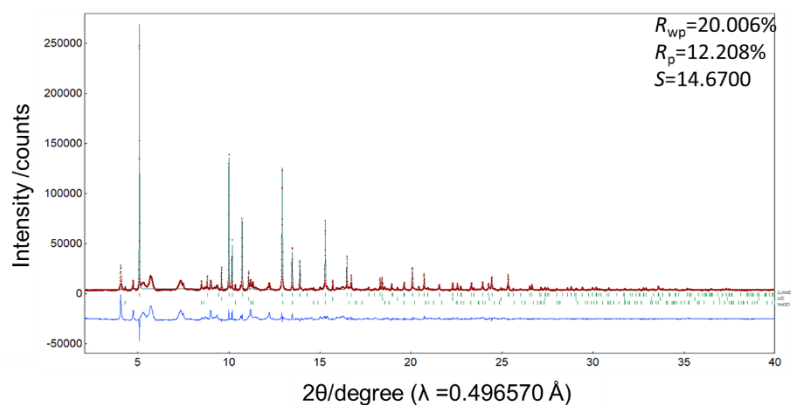
Fig. S1: Rietveld profile for S-Li₃HoCl₆. The experimental and calculated results are indicated by dots and solid lines, respectively. The green bars are the diffraction position of S-Li$_3$HoCl$_6$. The bottom lines are the residuals.

$R_{wp}=19.282\%$
$R_p=12.256\%$
$S=9.2430$
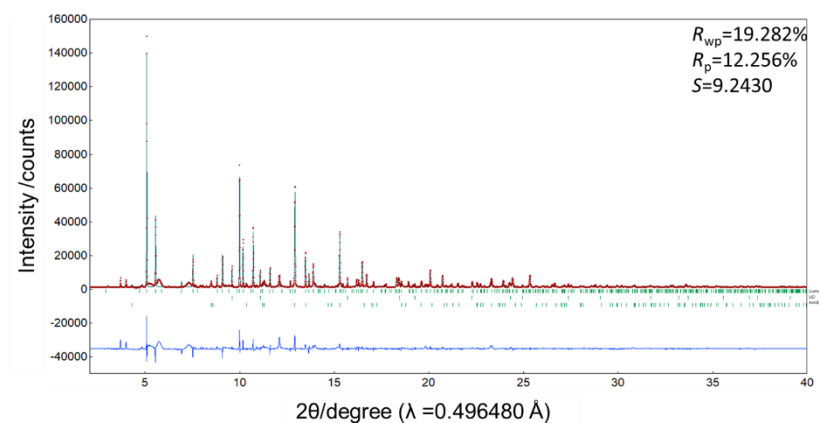
Fig. S2: Rietveld profile for T-Li₃HoCl₆. The experimental and calculated results are indicated by dots and solid lines, respectively. The green bars are the diffraction position of T-Li$_3$HoCl$_6$. The bottom lines are the residuals.

Table S2 Atoms, occupancies, atomic coordinates, and atomic displacement parameters of S-Li₃HoCl₆. The atomic coordinates and the atomic displacement parameter, U, were employed for Li. The occupancies of Ho converged into 0.50 within the error. The final refinement was performed with the fixed occupancies. The impurity phases were LiCl and HoOCl

Space group:165, $P\bar{3}c1$

Lattice Parameters: a= 6.46322 (15) Å, c=6.03367(16) Å.

Atom	Wyckoff position	Occupancy	Atomic coordinates			U /Å²
			x	y	z	
Ho	2b	0.5	0	0	0	0.0121(10)
Li	4d	0.75	1/3	2/3	0	0.01267(fixed)
Cl	6f	1	1/3	0	1/4	0.0258(15)

Table S3 Atoms, occupancies, atomic coordinates, and atomic displacement parameters of T-Li₃HoCl₆. The atomic coordinates and atomic displacement parameters, U, were employed for Li. The refined formula was $Li_3Ho_{0.98(3)}Cl_6$.

Space group:164, $P\bar{3}m1$

Lattice Parameters: a= 11.1941 (2) Å, c=6.03851(12) Å.

Atom	Wyckoff position	Occupancy	Atomic coordinates			U /Å²
			x	y	z	
Ho1	1a	0.88(2)	0	0	0	0.0153(10)
Ho2	1b	0.138(19)	0	0	1/2	=Ho1
Ho3	2d	0.632(13)	1/3	2/3	0.496(3)	=Ho1
Ho4	2d	0.328(12)	1/3	2/3	-0.017(5)	=Ho1
Li1	6g	0.75	0.34	0	0	0.03166(fixed)

Li2	6*h*	0.79	0.33	0	1/2	0.03166(fixed)
Cl1	6*i*	1	0.112(3)	-x	0.241(5)	0.0269(16)
Cl2	6*i*	1	0.778(2)	-x	0.267(5)	=Cl1
Cl3	6*i*	1	0.447(2)	-x	0.253(5)	=Cl1

The EXAFS spectra were analyzed using the ATHENA and ARTEMIS software packages[1]. EXAFS profiles were Fourier transformed in a range of the wave vector from 3 to 15 Å^{-1}, and the refinement was carried out for the Fourier transformed profile with a range from 1 to 6 Å. A result of the fitting and determined structure parameters of S-Li_3YCl_6 are shown in Fig. S3 and Table S4, respectively. Our model consists of eight single scattering paths for the bonds around Y atom with $R < 6$ Å. In our model, Debye-Waller factor of each bond was fitted independently, whereas the bond length was determined on the assumption of proportional variation with the expansion/compression of the lattice constant. The fitted profile well traces the experimental result of S-Li_3YCl_6 as shown in Fig. S3. The profile was reproduced by the component of Y-Cl bonds, whereas Y-Y and Y-Li bonds did not contribute to the profile apparently due to their large Debye-Waller factors, $\sigma^2 > 0.01$ Å^2. We note that the contribution from the nearest neighboring Y atom (Y-Y1) was too weak despite the large scattering capability of Y atom compared to those from Li and Cl atoms. The arrow in Fig. S3 indicates the expected position of the nearest-neighboring Y-Y bond, however, both a peak and shoulder structures seemed absent. This result is clear evidence that the nearest-neighboring Y-Y did not exist in the structure as discussed in the main text.

The Fourier transform of the EXAFS spectrum for S-Li_3HoCl_6 was also refined to investigate the local structure around Ho. The refinement which only included a scattering of Ho-Cl converged with moderate parameters as well as the results of Li_3HoCl_6. Furthermore, ΔE_0 became remarkably large ($\Delta E_0 > 25$ eV) when the scattering of Ho-Ho was employed, suggesting that the face-sharing nearest-neighbor octahedra were vacant. Thus, we concluded that the local structure of Li_3HoCl_6 was composed of the 1D atomic chain of alternately appearing Ho.
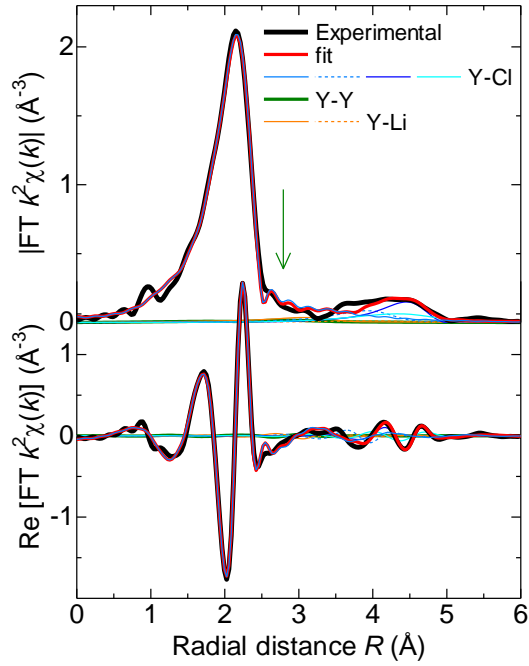
Fig. S3: Fitted and experimental Fourier transform profiles of S-Li₃YCl₆. Decomposed profile of each scattering path is shown together with the fitted and experimental profiles. The downward arrow indicates the expected position of Y-Y1 component.

Table S4 Fitted parameters of the local structure around Y atom determined by EXAFS at the Y K-edge. Coordination numbers, bond length, and Debye-Waller factors of the bonds around Y atom, σ^2, for S-Li₃YCl₆. Other fitted parameters: the overall amplitude reduction factor $S0$= 1.08(3) and correction of the absorption energy E_0, ΔE_0=0.4(3) eV. σ^2 of Y-Cl4 bond was not available due to its weak contribution.

Bond	Coordination number N	Bond length R /Å	Debye-Waller factors σ^2/Å^2
Y-Cl1	6	2.645(3)	0.0061(4)
Y-Y1	2	3.034(4)	0.05(6)
Y-Li1	6	3.753(4)	0.02(3)

Y-Cl2	6	4.592(5)	0.026(9)
Y-Li2	12	4.826(6)	0.04(5)
Y-Cl3	6	5.040(6)	0.013(4)
Y-Cl1	6	5.290(6)	0.04(1)
Y-Cl4	8	5.930(7)	N/A
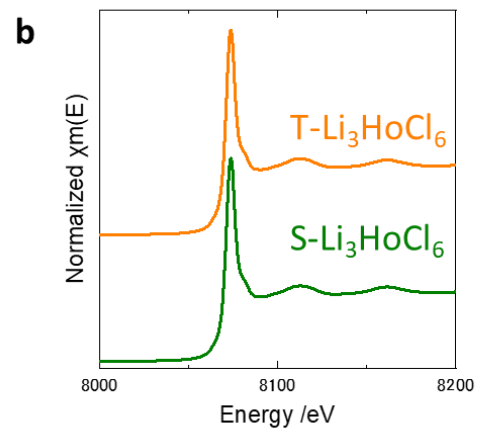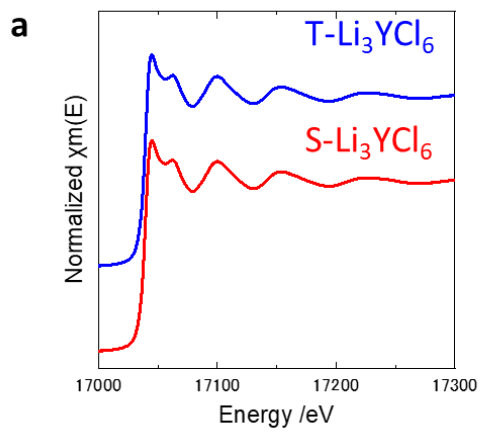
Fig. S4 (a)Y K-edge XAFS spectra of S- and T-Li_3YCl_6. (b) the Ho L_3-edge XAFS spectra of S- and T-Li_3HoCl_6. S- and T- Li_3MCl_6 showed similar spectra, indicating polymorphs of the same compositions crystalized with the same local structures.

Fig. S5 depicts the ^7Li NMR spectra in the range of the chemical shift from 100 to -100 ppm. The Spectra were corrected with magic angle spinning and normalized. The main peaks were observed around 0 ppm and two spinning sidebands were located at ±80 ppm. The peak shift was observed for polymorphs though the peak intensities of Li in Li_3HoCl_6 were weak due to the magnetism of Ho^{3+}.
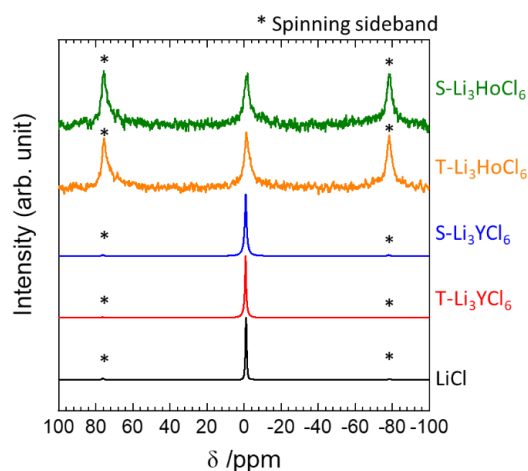
Fig. S5: Local structure of Li in Li₃MCl₆. The NMR spectra of S- and T- Li_3MCl_6 were collected with the magic angle spinning of 15 kHz. The spectrum of LiCl is shown as the reference of the peak position of Li.

Reference

1.   Ravel, B. & Newville, M. ATHENA, ARTEMIS, HEPHAESTUS: data analysis for X-ray absorption spectroscopy using IFEFFIT. *J. Synchrotron Radiat.* **12**, 537–541 (2005).